INTERNATIONAL JOURNAL FOR NUMERICAL METHODS IN FLUIDS
Int. J. Numer. Meth. Fluids 2000; **33**: 35–57

Two-dimensional dam break flow simulation

P. Brufau[1] and P. Garcia-Navarro*,[2]

Mecánica de Fluidos, Centro Politécnico Superior, Universidad de Zaragoza, María de Luna s/n, 50015 Zaragoza, Spain

SUMMARY

Numerical modelling of shallow water flow in two dimensions is presented in this work with the results obtained in dam break tests. Free surface flow in channels can be described mathematically by the shallow-water system of equations. These equations have been discretized using an approach based on unstructured Delaunay triangles and applied to the simulation of two-dimensional dam break flows. A cell centred finite volume method based on Roe's approximate Riemann solver across the edges of the cells is presented and the results are compared for first- and second-order accuracy. Special treatment of the friction term has been adopted and will be described. The scheme is capable of handling complex flow domains as shown in the simulation corresponding to the test cases proposed, i.e. that of a dam break wave propagating into a 45° bend channel (UCL) and in a channel with a constriction (LNEC-IST). Comparisons of experimental and numerical results are shown. Copyright © 2000 John Wiley & Sons, Ltd.

KEY WORDS: dam break flow; finite volume method; shallow-water equations; unstructured grid

1. INTRODUCTION

At present, classical methods and central difference schemes dominate the software products for the shallow-water system of equations. Some years after their adoption for solving problems in gas dynamics, upwind schemes have been successfully used for the solution of the shallow-water equations, with similar advantages [1–5]. Historically, upwind schemes were developed specifically for the solution of the Euler equations [6,7], but there is no reason why the techniques involved cannot be applied for the solution of other systems of conservation laws.

First-order and second-order schemes have been used to solve two-dimensional dam break flows on structured meshes following central differences [8] and upwind flux difference

* Correspondence to: Departamento de Ciencia y Tecnologia de Materiales y Fluidos, Area de Mecánica de Fluidos, Centro Politécnico Superior, Universidad de Zaragoza, María de Luna s/n, 50015 Zaragoza, Spain.
[1] E-mail: cuca@ideafix.litec.csic.es
[2] E-mail: pigar@posta.unizar.es

Received September 1998
Revised July 1999

approaches [1]. More recently, first- [9,10] and second-order [11] upwind schemes on unstructured meshes have been presented for this kind of flow. It is conjectured that the main reason for the relatively poor widespread of existing higher-order unstructured mesh schemes in the past has been due to the difficulty in constructing extensions to higher-order accuracy analogous to what has been done on structured meshes.

Upwind schemes are originally based on a piecewise constant representation of the solution on a cell and a one-dimensional Riemann solver across each edge of the cell. There are two main approaches for constructing positive higher-order schemes [6,12], which correspond to either flux or slope limiting. In this work, slope limiter functions are formulated directly, which gives quite a significant improvement when an unstructured finite volume scheme is applied with more ambitious reconstructions [13]. For a theoretical study on the convergence of higher-order upwind schemes on unstructured grids see Wierse [14].

Besides this, discussion is open as to whether the schemes based on one-dimensional Riemann solvers are the most suitable choice for multi-dimensional calculations because they seem inadequate for capturing two-dimensional flow features. Multi-dimensional upwinding techniques [15–18] have demonstrated to give very good resolution for dam break problems in genuinely two-dimensional domains [19], but their implementation is more complicated.

In this paper, the performance of an upwind technique for two-dimensional shallow-water flows is described in first- and second-order accuracy. In the next sections, the basis of the numerical method is stated; higher-order spatial accuracy is derived through the use of piecewise linear solution reconstruction over each element; special treatment of the friction term at the walls of the channel is described and the application to the simulation of two-dimensional dam break flows is presented.

2. GOVERNING EQUATIONS

Depth averaging of the free surface flow equations under the shallow-water hypothesis leads to a common version of the two-dimensional shallow-water equations, which in conservative form [20,21] is

$$\frac{\partial \mathbf{U}}{\partial t} + \nabla \cdot (\mathbf{F}, \mathbf{G}) = \mathbf{H} \tag{1}$$

with

$$\mathbf{U} = \begin{pmatrix} h \\ hu \\ hv \end{pmatrix}, \qquad \mathbf{F} = \begin{pmatrix} hu \\ hu^2 + g\dfrac{h^2}{2} \\ huv \end{pmatrix}, \qquad \mathbf{G} = \begin{pmatrix} hv \\ huv \\ hv^2 + g\dfrac{h^2}{2} \end{pmatrix},$$

$$\mathbf{H} = \begin{pmatrix} 0 \\ gh(S_{0_x} - S_{f_x}) \\ gh(S_{0_y} - S_{f_y}) \end{pmatrix} \tag{2}$$

where **U** represents the vector of conserved variables (h is the depth of water, hu and hv are unit discharges along the co-ordinate directions), **F** and **G** are the fluxes of the conserved variables across the edges of a control volume. They consist of the convective fluxes together with the hydrostatic pressure gradients. **H** is the source term.

In addition, u and v are the velocities in the x- and y-directions respectively, g is the acceleration due to the gravity, S_{0_x} and S_{0_y} are the bed slopes, and S_{f_x} and S_{f_y} are the friction terms in the x- and y-directions respectively. For the friction term, the Manning equation [22] has been used with some modifications and will be described in Section 4.

For the present applications other source terms, apart from wall and bottom friction and weight of the fluid, have been neglected. Hence, no turbulent dissipation terms, Coriolis or wind effect are present in the equations.

Despite the apparent restricted application of this mathematical model of the free surface flow, it has been widely used for numerical simulations of hydraulic phenomena [21]. Dam break induced flows in particular are one example of common application. Even though the hydraulic hypothesis is violated at the dam position during dam failure and at the shock front during its propagation, the shallow-water model still remains valid as an average description of the main features of this kind of transient flow.

In the next section, the numerical techniques applied to solve Equation (1) are described.

3. NUMERICAL MODEL

3.1. First-order upwind method

A cell centred finite volume method is formulated for Equation (1) over a triangular control volume, where the dependent variables of the system are represented as piecewise constants. The integral form of Equation (1) for a fixed area S is

$$\int_S \frac{\partial \mathbf{U}}{\partial t}\,\mathrm{d}S + \int_S \nabla\cdot(\mathbf{F},\mathbf{G})\,\mathrm{d}S = \int_S \mathbf{H}\,\mathrm{d}S \tag{3}$$

and applying the divergence theorem to the second integral, you obtain

$$\int_S \frac{\partial \mathbf{U}}{\partial t}\,\mathrm{d}S + \oint_C (\mathbf{F},\mathbf{G})\cdot\mathbf{n}\,\mathrm{d}C = \int_S \mathbf{H}\,\mathrm{d}S \tag{4}$$

where C is the boundary of the area S, and **n** is the outward unitary normal vector. Given a computational mesh defined by the cells (volumes) of area S_i, where i is the index associated with the centroid of the cell (see Figure 1) in which the cellwise constant values of **U** are stored, Equation (4) can be represented by

$$\frac{\mathrm{d}U_i}{\mathrm{d}t} S_i + \oint_{C_i} (\mathbf{F},\mathbf{G})\cdot\mathbf{n}\,\mathrm{d}C = \mathbf{H}_i S_i \tag{5}$$

where a mesh fixed in time is assumed. The contour integral is approached via a mid-point rule, i.e. a numerical flux is defined at the mid-point of each edge, giving

$$\oint_{C_i} (\mathbf{F}, \mathbf{G})\cdot\mathbf{n}\, \mathrm{d}C = \sum_{k=1}^{NE} (\mathbf{F}, \mathbf{G})^*_{w_k}\cdot\mathbf{n}_{w_k}\, \mathrm{d}C_{w_k} \tag{6}$$

where w_k represents the index of edge k of the cell (see Figure 1), NE is the total number of edges in the cell ($NE = 3$ for triangles). The vector $\mathbf{n}_{w_k}$ is the unit outward normal, $\mathrm{d}C_{w_k}$ is the length of the side, and $(\mathbf{F}, \mathbf{G})^*_{w_k}$ is the numerical flux tensor.

The evaluation of the numerical flux in Equation (6) is based on the Riemann problem defined by the conditions on the left and right sides of the cell edges, as in first-order method of extrapolation of variables scheme [23]. An important feature of the one-dimensional upwind schemes for non-linear systems of equations is exploited here. This is the definition of the approximated flux Jacobian, $\tilde{A}_{i+1/2}$ [7], constructed at the edges of the cells. Once this matrix has been defined, the numerical flux across the interface $i+\frac{1}{2}$ between states i on the left (L) and $i+1$ on the right (R) of a cell in a one-dimensional domain is

$$\mathbf{F}^*_{i+1/2} = \frac{1}{2}[\mathbf{F}_{i+1} + \mathbf{F}_i - |\tilde{\mathbf{A}}_{i+1/2}|(\mathbf{U}_{i+1} - \mathbf{U}_i)] = \frac{1}{2}[\mathbf{F}_\mathrm{R} + \mathbf{F}_\mathrm{L} - |\tilde{\mathbf{A}}_\mathrm{RL}|(\mathbf{U}_\mathrm{R} - \mathbf{U}_\mathrm{L})] \tag{7}$$

The two-dimensional numerical upwind flux in Equation (6) is obtained by applying the expression (7) in a one-dimensional form to each edge w_k of the computational cell. The one-dimensional philosophy is followed along the normal direction to the cell walls, making use of the normal numerical fluxes, so that

$$(\mathbf{F}, \mathbf{G})^*\cdot\mathbf{n} = \frac{1}{2}[(\mathbf{F}, \mathbf{G})_\mathrm{R}\cdot\mathbf{n} + (\mathbf{F}, \mathbf{G})_\mathrm{L}\cdot\mathbf{n} - |\tilde{\mathbf{A}}_\mathrm{RL}|(\mathbf{U}_\mathrm{R} - \mathbf{U}_\mathrm{L})] \tag{8}$$

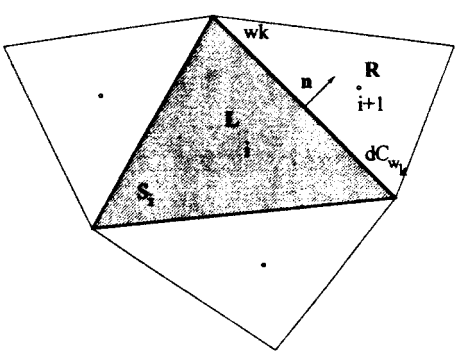

Figure 1. Details of the cells.

Here $k = 1, \ldots, NE$. R and L denote the right and the left states respectively at the w_k edge, $\tilde{\mathbf{A}}_{\mathrm{RL}}$ represents the approximate Jacobian of the normal flux. Note that subscript w_k will be omitted for the sake of clarity and the following discussion is referred to the cell side w_k.

The $\tilde{\mathbf{A}}_{\mathrm{RL}}$ matrix must satisfy the following conditions:

(I) $\tilde{\mathbf{A}}_{\mathrm{RL}}$ depends only on the $\mathbf{U}_{\mathrm{R}}$ and $\mathbf{U}_{\mathrm{L}}$ states,
(II) $(\mathbf{F}_{\mathrm{R}} - \mathbf{F}_{\mathrm{L}}) = \tilde{\mathbf{A}}_{\mathrm{RL}}(\mathbf{U}_{\mathrm{R}} - \mathbf{U}_{\mathrm{L}})$,
(III) $\tilde{\mathbf{A}}_{\mathrm{RL}}$ has real and distinct eigenvalues and a complete set of eigenvectors,
(IV) $\tilde{\mathbf{A}}_{\mathrm{RL}} = \mathbf{A}(\mathbf{U}_{\mathrm{R}}) = \mathbf{A}(\mathbf{U}_{\mathrm{L}})$ if $\mathbf{U}_{\mathrm{R}} = \mathbf{U}_{\mathrm{L}}$,

where

$$\mathbf{A} = \frac{\partial(\mathbf{F}, \mathbf{G})}{\partial \mathbf{U}}\mathbf{n} = \frac{\partial \mathbf{F}}{\partial \mathbf{U}}n_x + \frac{\partial \mathbf{G}}{\partial \mathbf{U}}n_y \tag{9}$$

As suggested by Roe [7], the matrix $\tilde{\mathbf{A}}_{\mathrm{RL}}$ has the same shape as $\mathbf{A}$ but is evaluated at an average state given by the quantities $\tilde{\mathbf{u}} = (\tilde{u}, \tilde{v})$ and $\tilde{c}$, which must be calculated according to the matrix properties. The eigenvalues of $\tilde{\mathbf{A}}_{\mathrm{RL}}$ have the form

$$\tilde{a}^1 = \tilde{\mathbf{u}}\cdot\mathbf{n} + \tilde{c}$$

$$\tilde{a}^2 = \tilde{\mathbf{u}}\cdot\mathbf{n}$$

$$\tilde{a}^3 = \tilde{\mathbf{u}}\cdot\mathbf{n} - \tilde{c} \tag{10}$$

where $\tilde{\mathbf{u}}\cdot\mathbf{n} = \tilde{u}n_x + \tilde{v}n_y$, and the eigenvectors are

$$\tilde{\mathbf{e}}^1 = \begin{pmatrix} 1 \\ \tilde{u} + \tilde{c}n_x \\ \tilde{v} + \tilde{c}n_y \end{pmatrix}, \qquad \tilde{\mathbf{e}}^2 = \begin{pmatrix} 0 \\ -\tilde{c}n_y \\ \tilde{c}n_x \end{pmatrix}, \qquad \tilde{\mathbf{e}}^3 = \begin{pmatrix} 1 \\ \tilde{u} - \tilde{c}n_x \\ \tilde{v} - \tilde{c}n_y \end{pmatrix} \tag{11}$$

Once the eigenvalues and eigenvectors are calculated, the difference in the vector $\mathbf{U}$ across a grid edge is decomposed on the eigenvectors basis as

$$\delta\mathbf{U} = \mathbf{U}_{\mathrm{R}} - \mathbf{U}_{\mathrm{L}} = \sum_{m=1}^{3} \alpha_{\mathrm{RL}}^m \tilde{\mathbf{e}}_{\mathrm{RL}}^m \tag{12}$$

where

$$\alpha_{\mathrm{RL}}^{1,3} = \frac{\delta h_{\mathrm{RL}}}{2} \pm \frac{1}{2\tilde{c}}\left[\delta(hu)_{\mathrm{RL}}n_x + \delta(hv)_{\mathrm{RL}}n_y - \tilde{\mathbf{u}}\cdot\mathbf{n}\delta h_{\mathrm{RL}}\right]$$

$$\alpha_{\mathrm{RL}}^{2} = \frac{1}{\tilde{c}}\left[(\delta(hv)_{\mathrm{RL}} - \tilde{v}\delta h_{\mathrm{RL}})n_x - (\delta(hu)_{\mathrm{RL}} - \tilde{u}\delta h_{\mathrm{RL}})n_y\right] \tag{13}$$

Enforcing the second condition of matrix $\tilde{\mathbf{A}}_{\mathrm{RL}}$, the following expressions for $\tilde{u}$, $\tilde{v}$ and $\tilde{c}$ can be obtained:

$$\tilde{u} = \frac{\sqrt{h_{\mathrm{R}}}u_{\mathrm{R}} + \sqrt{h_{\mathrm{L}}}u_{\mathrm{L}}}{\sqrt{h_{\mathrm{R}}} + \sqrt{h_{\mathrm{L}}}}, \qquad \tilde{v} = \frac{\sqrt{h_{\mathrm{R}}}v_{\mathrm{R}} + \sqrt{h_{\mathrm{L}}}v_{\mathrm{L}}}{\sqrt{h_{\mathrm{R}}} + \sqrt{h_{\mathrm{L}}}}, \qquad \tilde{c} = \sqrt{\frac{g}{2}(h_{\mathrm{R}} + h_{\mathrm{L}})} \tag{14}$$

Once the average quantities have been constructed, expression (8) provides the numerical flux normal to each edge of the computational cells. We can now substitute it into Equation (6), so that Equation (5) can be written as

$$\frac{\mathrm{d}\mathbf{U}_i}{\mathrm{d}t} = -\frac{1}{S_i}\sum_{k=1}^{NE}(\mathbf{F}, \mathbf{G})^*_{w_k} \cdot \mathbf{n}_{w_k}\,\mathrm{d}C_{w_k} + \mathbf{H}_i \tag{15}$$

which is an ordinary differential equation and can be integrated by standard methods, such as a forward Euler time integration procedure,

$$\mathbf{U}_i^{n+1} = \mathbf{U}_i^n - \frac{\Delta t}{S_i}\left(\sum_{k=1}^{NE}(\mathbf{F}, \mathbf{G})^*_{w_k} \cdot \mathbf{n}_{w_k}\,\mathrm{d}C_{w_k}\right)_i^n + \Delta t\,\mathbf{H}_i^n \tag{16}$$

The stability criterion adopted has followed the usual in explicit finite volumes [24]

$$\delta t \leq \min\left[\frac{d_{ij}}{2(\sqrt{u^2 + v^2} + c)_{ij}}\right] \tag{17}$$

where d_{ij} is the distance between the centroid of the cell i and its neighbours j.

3.2. Second order extension

A first-order-accurate upwind scheme has been constructed computing the fluxes at each face from the adjacent piecewise constant values of the variables $\mathbf{U}$ in each volume. In order to obtain higher-order spatial accuracy, the initial data at each time step are pre-processed in the form

$$\mathbf{U}_{\mathrm{L}} \Rightarrow \mathbf{U}_{\mathrm{L}} + \mathbf{r}_{\mathrm{LR}}D_{\mathrm{L}}, \qquad \mathbf{U}_{\mathrm{R}} \Rightarrow \mathbf{U}_{\mathrm{R}} + \mathbf{r}_{\mathrm{RL}}D_{\mathrm{R}} \tag{18}$$

where $\mathbf{r}_{\mathrm{LR}}$ is the vector from the centroid of the cell L to the mid-point of the edge LR (see Figure 2). The new left and right values of the variables are two interpolated values constructed from the initial constant values and situated at the mid-point of the edge from the centroids of elements L and R respectively.

The representation of the initial conditions for the Riemann solver is now different since it contains information relative to the neighbour cells by means of the gradient operator D.

The construction of the gradient operator D is of crucial importance to the numerical scheme. It has to be conservative and guarantee positivity [13,14]. The limited central difference (LCD) approach, the compressive limiter of Durlofsky *et al.* [25] and the maximum

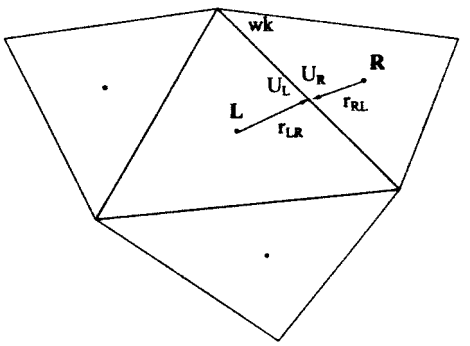

Figure 2. Details of the cells.

limiter gradient (MLG) operator, described in detail here, have been studied following Batten *et al.*'s previous work [13]. Only results with the MLG operator are going to be shown in this work.

The procedure for the non-oscillatory reconstructions of the initial piecewise constant values can be extended to an arbitrary cell shape; here triangles are considered. Given the three centroids A, B and C of the adjacent cells to one of the triangles (with centroid O), as shown in Figure 3, a unique gradient plane can be defined from

$$D = \begin{pmatrix} -\mathbf{m}^2/\mathbf{m}^3 \\ -\mathbf{m}^1/\mathbf{m}^3 \end{pmatrix} \tag{19}$$

where $\mathbf{m}^k$ ($k = 1, 2, 3$) is the k component of the normal vector to the plane (ABC), given by

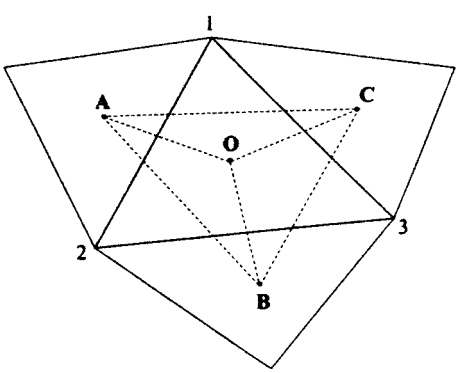

Figure 3. Details of the cells.

$$\mathbf{m}^k = \left(\begin{bmatrix} x \\ y \\ \mathbf{U}^k \end{bmatrix}_C - \begin{bmatrix} x \\ y \\ \mathbf{U}^k \end{bmatrix}_A \right) \times \left(\begin{bmatrix} x \\ y \\ \mathbf{U}^k \end{bmatrix}_C - \begin{bmatrix} x \\ y \\ \mathbf{U}^k \end{bmatrix}_B \right) \tag{20}$$

The algorithm implemented is the following:

Construction of the operators D^i, $i = 1, 2, 3, 4$.
To determine the gradient operator D on an unstructured triangular mesh, at least four gradient planes through a triangle, given the centroid of the triangle itself and the centroids of the three adjacent triangles, which have one edge in common, can be defined (see Figure 3)

$$D^1 = \triangle(123), \qquad D^2 = \triangle(ABO), \qquad D^3 = \triangle(BCO), \qquad D^4 = \triangle(CAO)$$

where $\triangle(ABO)$ defines the unique gradient plane through the centroids A, B and O. Limiting condition over the gradient operators D^i by a scalar α_i such that $D^i = \alpha_i \cdot D^i$, where $0 \leq \alpha \leq 1$, and α is maximized subject to the constraint that the solution causes no overshoots or undershoots at cell interfaces. This is imposed to prevent non-physical extreme. The MLG algorithm moderates all gradients.
Once we assure none of the D^i can cause overshoots/undershoots, the operator D^i that gives maximum compression ($|D^i|$ maximum) is selected. This limiter automatically selects a zero gradient at points of extreme. It has been demonstrated that the MLG slope limiter corresponds to the one-dimensional Superbee limiter of Roe [26].

Second-order spatial accuracy is obtained proceeding as has been explained before, with the slope limiter on the variables using the MLG gradient operator in order to define $\mathbf{U}_L$ and $\mathbf{U}_R$ in Equations (8) and (16). Second-order accuracy in time can be achieved from Equation (15) updating the variables in two steps. In the first step, variables are computed at time level $t^{n+1/2} = t^n + \Delta t/2$ from the extrapolated variables at time t^n. With these values, the numerical flux and the source terms are evaluated again to update the variables at time t^{n+1},

$$\mathbf{U}_i^{n+1/2} = \mathbf{U}_i^n - \frac{\Delta t}{2S_i} \left(\sum_{k=1}^{NE} (\mathbf{F}, \mathbf{G})_{w_k}^* \cdot \mathbf{n}_{w_k} \, \mathrm{d}C_{w_k} \right)^n + \frac{\Delta t}{2} \mathbf{H}_i^n$$

$$\mathbf{U}_i^{n+1} = \mathbf{U}_i^n - \frac{\Delta t}{S_i} \left(\sum_{k=1}^{NE} (\mathbf{F}, \mathbf{G})_{w_k}^* \cdot \mathbf{n}_{w_k} \, \mathrm{d}C_{w_k} \right)^{n+1/2} + \Delta t \mathbf{H}_i^{n+1/2} \tag{21}$$

3.3. Source terms

Many two-dimensional depth-averaged models include only friction at the bottom. Specifically, models that assume vertical channel side-walls and use free-slip boundary conditions do not account for the friction at the walls. Neglecting this effect, open channel flow would likely show a marked variation in water depth [27] from the one measured experimentally.

Evaluation of the friction slope that quantifies the energy loss at the side-walls of the channel is required. It is common to use a uniform flow law, Manning or Chezy formulae, to calculate this term. However, these laws were developed for one-dimensional flow and must be extended and properly incorporated to two-dimensional equations.

Manning's formula used in one-dimensional shallow-water models is expressed in the form

$$S_f = \frac{n^2 Q|Q|}{A^2 R^{4/3}} \tag{22}$$

where n is the Manning coefficient and $R = A/P$ is the hydraulic radius, which depends on the wetted perimeter P. For a rectangular channel $P = b + 2h$ and for an irregular basin $P = b$.

A distinction must be made between an arbitrary channel cross-section and a cross-section with vertical walls (see Figure 4). Most two-dimensional models assume vertical walls and free-slip wall boundary conditions for rectangular channels, while the equations used to compute the friction term are based on irregular cross-sections. To correct this inconsistency, the friction slope equation has been modified here to reflect the vertical side-wall assumption. Basically, the modification ensures that the entire wetted perimeter (bottom width and side-walls) is accounted for.

For an arbitrary cross-section, the wetted perimeter in a cell is equal to the bottom width b (see Figure 4), so that the hydraulic radius adopts the form $R = h$, the water depth. In this case, the two-dimensional friction terms are written in the form [28–31]

$$S_{f_x} = \frac{n^2 u\sqrt{u^2 + v^2}}{h^{4/3}}, \qquad S_{f_y} = \frac{n^2 v\sqrt{u^2 + v^2}}{h^{4/3}} \tag{23}$$

When these formulae are applied to rectangular channels with free-slip wall boundary conditions, only bottom friction is taken into account, neglecting the side-walls friction (see Figure 4).

Working with structured meshes, Molls *et al.* [27] modified the friction slope equation distributing the side-wall friction across the width of the channel. Every cell augments its wetted area in the form $S_i + (h_1 + h_N)/(N - 1)$, where N is the number of computational nodes across the channel, and h_1 and h_N are the water depths at the channel side-walls. Moreover, in Equation (23) a weighting factor is included that accounts for side-wall friction and can be viewed as a correction to the Manning coefficient n.

On unstructured meshes, there is no row of cells numbered from 1 to N in a cross-section and the above modification is not valid. The idea is to include the effect of the side-wall

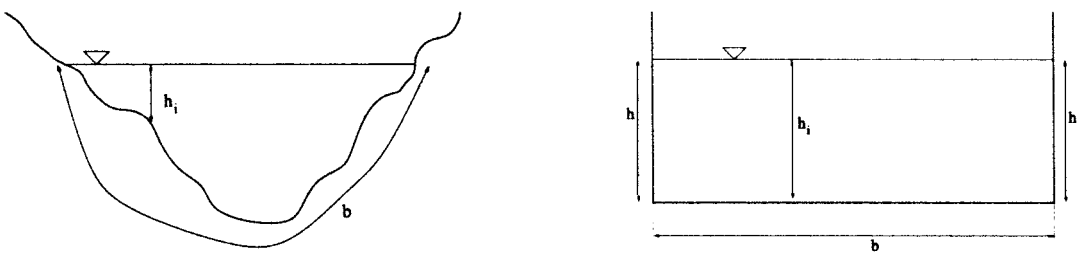

Figure 4. Irregular and rectangular cross sections.

friction in the computation of the total friction term in each cell, depending on the number of edges that form part of a vertical solid wall and computing the real wetted area (bottom and wall; see Figure 5).

Two different types of cells are distinguished: *internal* cells, where all the edges are adjacent to another cell; and *boundary* cells, where at least one of the edges is a vertical wall. For *internal* cells the procedure is the usual, with the Manning coefficient of the bottom, n_b,

$$S_{f_x} = \frac{n_b^2 u\sqrt{u^2+v^2}}{h^{4/3}}, \qquad S_{f_y} = \frac{n_b^2 v\sqrt{u^2+v^2}}{h^{4/3}} \tag{24}$$

For *boundary* cells, the wetted area must be specified. First of all, the total number of edges in a cell, which are part of solid vertical walls, is needed (SW N). The wetted area is $S_i + l_{w_k} h$ (see Figure 5), where S_i is the area of the cell, l_{w_k} is the length of the solid wall edge involved in this cell, and h is the depth of the water.

Equation (23) can be expressed in the form

$$S_{f_x} = u\sqrt{u^2+v^2}\left(\frac{n^{2/3}}{R}\right)^{4/3} \tag{25}$$

which gives the following expression for the friction term:

$$S_{f_x} = u\sqrt{u^2+v^2}\left(\frac{n_b^{2/3}}{h} + \sum_{w_k=1}^{\mathrm{SW}\ N} \frac{n_w^{3/2} l_{w_k}}{S_i}\right)^{4/3}, \qquad S_{f_y} = v\sqrt{u^2+v^2}\left(\frac{n_b^{2/3}}{h} + \sum_{w_k=1}^{\mathrm{SW}\ N} \frac{n_w^{3/2} l_{w_k}}{S_i}\right)^{4/3} \tag{26}$$

with n_w being the Manning coefficient relative to the vertical walls. The Manning coefficients for bottom and walls, n_b and n_w, used in the computations have been supplied by the experimental tests.

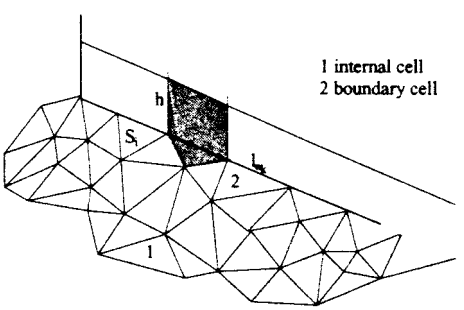

Figure 5. Wetted perimeter on a cell for a rectangular cross section.

Comparisons have been carried out using the standard friction slope formula neglecting the side-walls effect (23) and the modified law (26). Using Equation (26), numerical results agreed closer to the experimental data than with using the standard equation, better solving the arrival time of the reflected water from the walls. This modification works well with complex flows, such as curved channels and channels with contractions as will be shown in the numerical results.

3.4. Boundary conditions

The idea of using a Riemann solver to calculate the flux at the face of a cell can be used in the description of boundary conditions. The variables are stored at the centre of each cell and the boundary conditions are applied through the flux across the edges. The imposed conditions at the boundaries combined with equations obtained from characteristics theory give sufficient information for the boundary flux to be calculated.

We have applied characteristics theory [24] in two dimensions, the procedure consisting of the approximation of the bi-characteristics that pass through the boundary points. Assuming that we can neglect the source terms and that the flux has a frontal behaviour, we arrive at the following compatibility relations:

$$\frac{\mathrm{D}}{\mathrm{D}t}(\mathbf{u}\cdot\mathbf{n} \pm 2c) = 0 \tag{27}$$

$$\frac{\delta}{\delta t}(\mathbf{u}\cdot\mathbf{t}) = 0 \tag{28}$$

where $\mathbf{t}$ is the tangential vector,

$$\mathbf{u}\cdot\mathbf{n} = un_x + vn_y, \qquad \mathbf{u}\cdot\mathbf{t} = vn_x - un_y \tag{29}$$

and

$$\frac{\mathrm{D}}{\mathrm{D}t} = \frac{\partial}{\partial t} + (u \pm cn_x)\frac{\partial}{\partial x} + (v \pm cn_y)\frac{\partial}{\partial y} \tag{30}$$

$$\frac{\delta}{\delta t} = \frac{\partial}{\partial t} + u\frac{\partial}{\partial x} + v\frac{\partial}{\partial y} \tag{31}$$

Sometimes it is not necessary to use all the equations, depending on the boundary conditions imposed and the number being determined by the value of the normal velocity through the boundary. The possibilities are

(I) Supercritical inflow: $\mathbf{u}\cdot\mathbf{n} \leq -c \Rightarrow$ all the variables must be imposed and no numerical boundary conditions are needed.
(II) Sub-critical inflow: $-c < \mathbf{u}\cdot\mathbf{n} \leq 0 \Rightarrow$ two variables must be imposed and one of the two expressions included in Equation (27) is used.

(III) Supercritical outflow: $\mathbf{u}\cdot\mathbf{n} > c \Rightarrow$ none of the variables must be imposed and Equations (27) and (28) are used.
(IV) Sub-critical outflow: $0 < \mathbf{u}\cdot\mathbf{n} \leq c \Rightarrow$ one variable must be imposed and Equation (27) is used.

For instance, when the boundary is a solid wall, the normal velocity is zero, so it is necessary to use Equations (27) and (28), imposing the condition $\mathbf{u}\cdot\mathbf{n} = 0$.

Once boundary conditions have been imposed on the cell edges and have been combined with the appropriate compatibility relations, the normal flux across these edges is calculated and the contribution to the updating of the variables at the centre of the cell is obtained.

A useful remark must be done about the treatment of boundary conditions in the numerical modelling. Only first-order accuracy is achieved at the boundary cells due to the approximations assumed, even when a second-order scheme is applied. This opens a new path to study how boundary conditions treatment could be improved to obtain better accuracy on the results.

4. NUMERICAL RESULTS

Results obtained with both first- and second-order approximations for the experimental test cases proposed by Professor Zech (Civil Engineering Department, UCL, Belgium) and Dr Bento (Hydraulic Engineering Department, LNEC and IST, Lisbon) from the Working Group on Dam Break Flow Modelling, are going to be presented.

Experimental data obtained on a laboratory test facility for dam break unsteady flows will be compared with computational results obtained with first- and second-order accuracy numerical schemes on unstructured Delaunay triangular meshes. Initially, dry and wet bed tests have been carried out. Only results on wet bed cases, presenting more differences from experimental results than dry bed ones, are going to be shown. In general, flow over dry bed progresses with a smooth front wave and does not generate sharp fronts.

4.1. 45° bend channel test (UCL)

The test to be studied combines a square-shaped upstream reservoir and a 45° bend channel (see Figure 6). The flow will be essentially two-dimensional in the reservoir and at the angle between the two straight reaches of the 45° bend channel. Two features of the dam break resulting flow are of special interest: the damping effect of the corner, and the upstream moving hydraulic jump, which is formed by reflection at the corner. The multiple reflections of the expansion wave in the reservoir will also offer an opportunity to test the two-dimensional capabilities of the numerical models.

The channel is made of 4.25 and 4.15 m long and 0.495 m wide rectilinear reaches connected at 45° angle by an element. There is no slope in the channel. A gate connects this 45° bend channel to a $2.44 \times 2.39\ \mathrm{m}^2$ reservoir.

The initial conditions are water at rest with the free surface 0.25 m above the bed level in the upstream reservoir and 0.01 m water depth in the channel. All boundaries are solid non-slip walls except the outlet, which is considered free (supercritical). The Manning coefficient for the

bed is $n_b = 0.0095$ and $n_w = 0.0195$ for the walls. The number of elements used in the mesh is 15397.

Nine gauging points were used in the laboratory to measure water level in time. Their locations are shown in Figure 6. The measurements at these stations are compared with the numerical results and displayed in Figures 7 and 8. Both schemes give satisfactory solutions; first-order gives a smoother solution, and the reflections at the walls of the channel are better captured with second-order.

We would like to remark the improvement achieved taking into account the vertical channel side-walls when evaluating the friction term. Figure 7 shows the differences on the results when the effect of the side-walls friction is neglected (no wall friction) or not (wall friction). Figure 7(left) represents the water depth evolution at point P3, and only if the wall friction is

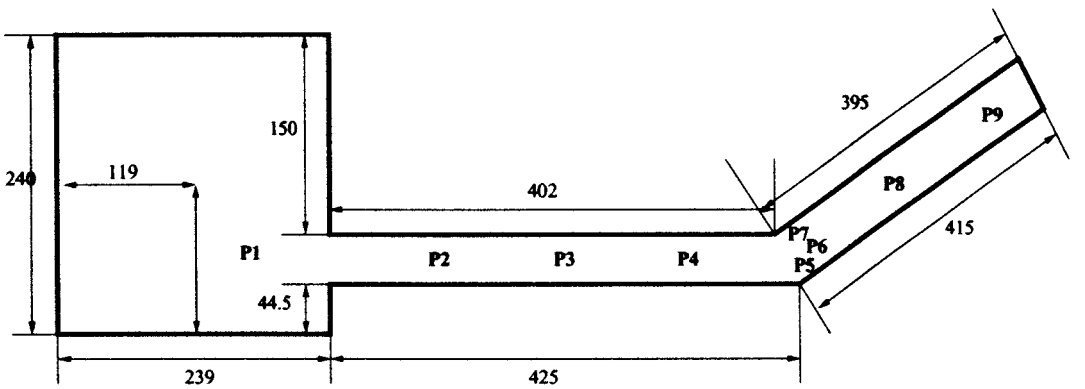

Figure 6. Plane view of the channel.

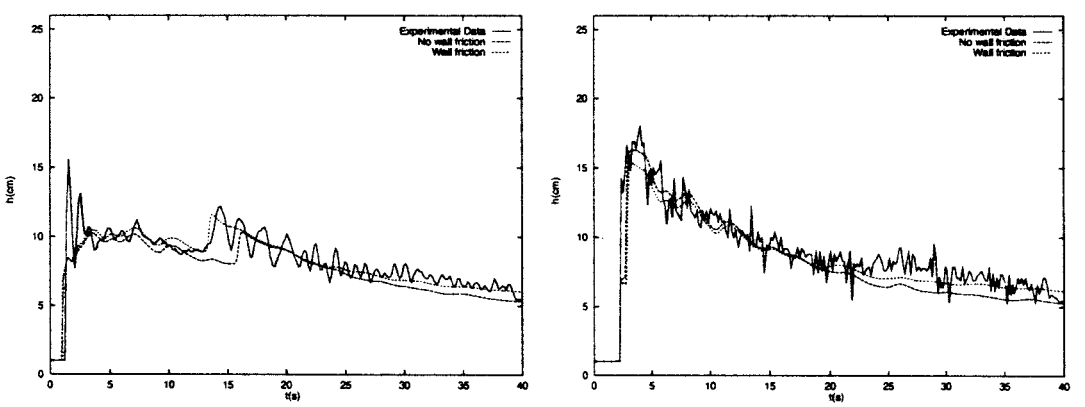

Figure 7. Water depth history at points P3 (left) and P5 (right).

considered the reflected front is captured at the correct time, otherwise it is delayed 3 s. At point P5 [Figure 7(right)] a better fit to the measurements has been noticed. From now on, the side-walls friction has been included in all the numerical computations.

Comparison between experimental data and numerical results obtained with first- and second-order upwind schemes are shown. Figure 8 represents the time evolution of the depth of water in nine gauging points along the structure (see Figure 6). In Figure 9 the water level contour along the channel is described at times 3 and 18 s. Finally, Figure 10 represents the snapshots of the free surface at the same time.

In general, the figures indicate a good performance of the two numerical schemes. Experimental data in this test show a remarkable oscillatory character. This behaviour cannot be modelled by means of a shallow water approach. The results from the second-order numerical scheme present less numerical diffusion than the ones provided by the first-order method but they still do not achieve a full agreement. The arrival times of the main shock fronts are well captured by both methods. Some differences are noticeable in P2, P3 and P4 as the reflected

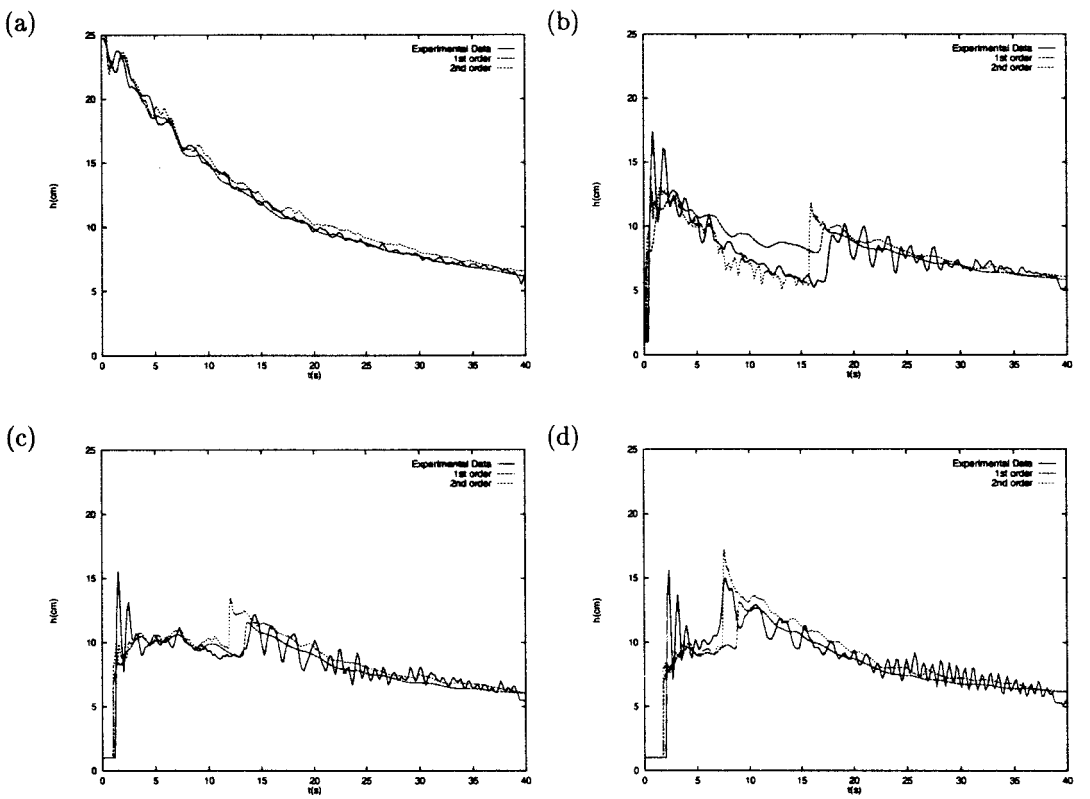

Figure 8. Water depth history at points (a) P1, (b) P2, (c) P3, (d) P4, (e) P5, (f) P6, (g) P7, (h) P8, and (i) P9.

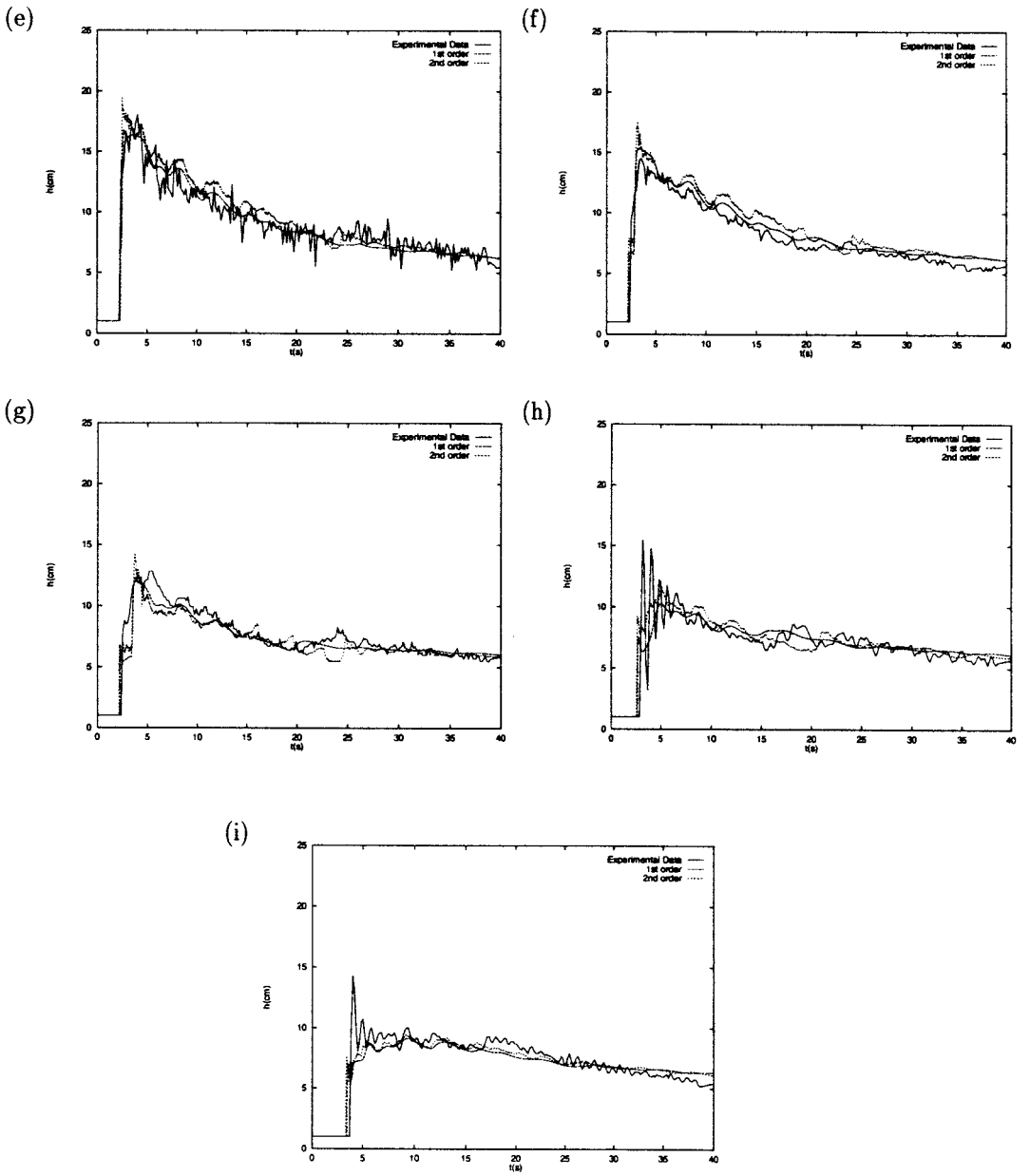

Figure 8 (*Continued*)

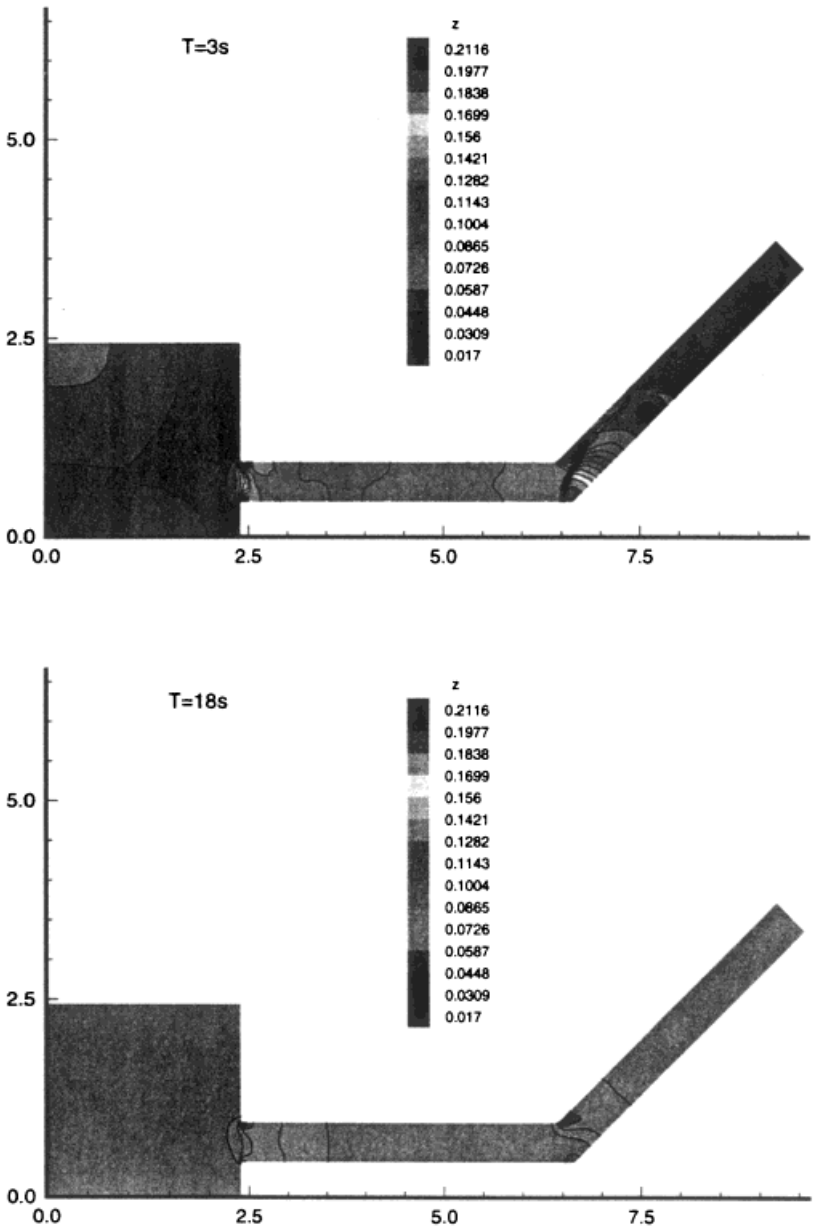

Figure 9. Contour of water level along the channel at time $t = 3$ s (top) and $t = 18$ s (bottom).

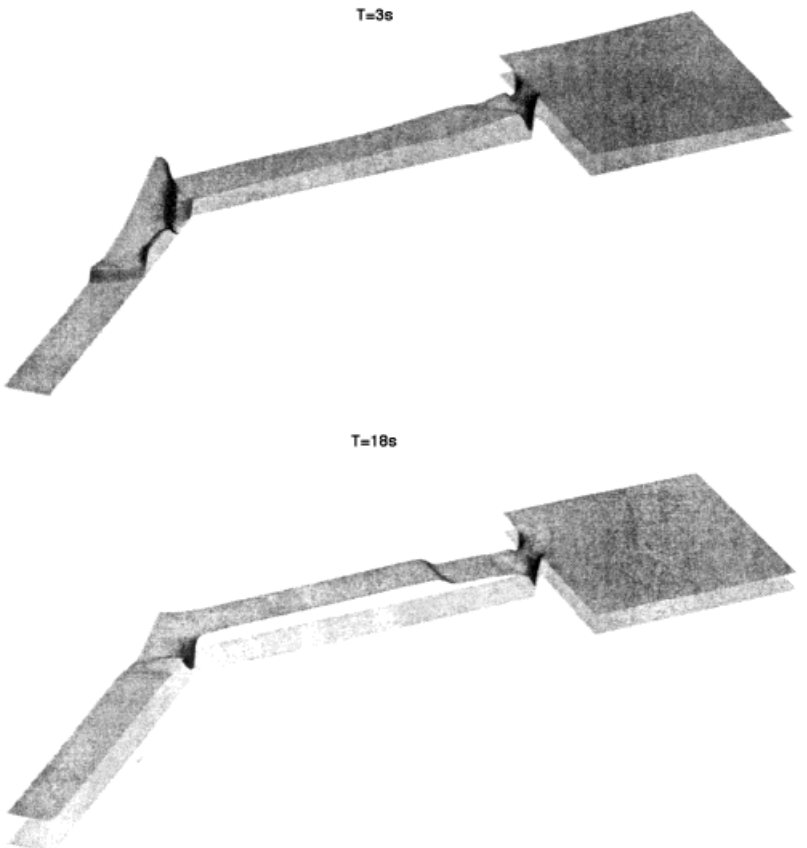

Figure 10. Free surface at time $t = 3$ s (top) and $t = 18$ s (bottom).

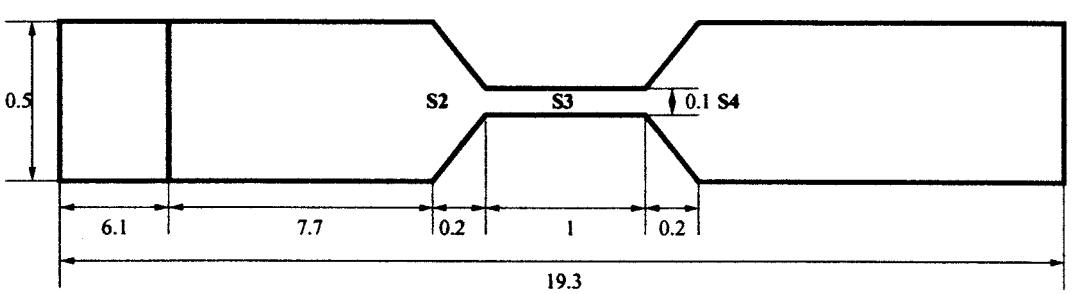

Figure 11. Plane view of the channel.

shock front celerity is concerned. This may be attributed to the treatment of the boundary conditions. The simplifications made in the numerical implementation of the characteristics theory in two-dimensional at the boundaries may be responsible for this lack of accuracy.

4.2. Channel with a constriction (LNEC-IST)

The entire channel, with a zero longitudinal slope, is 19.3 m long and its rectangular section is 0.5 m wide. The gate is located at 6.1 m from the upstream section of the channel. The upstream channel is also 0.5 m wide. The beginning of the constriction is located at 7.7 m downstream of the gate. The constriction is 1 m long and 0.1 m wide. The transition wall makes a 45° angle with the channel walls (see Figure 11).

The test was conducted with initial still water. The initial water depths are 0.397 m and 0.25 m. Boundary conditions are the same specified in the first test. The Manning coefficient

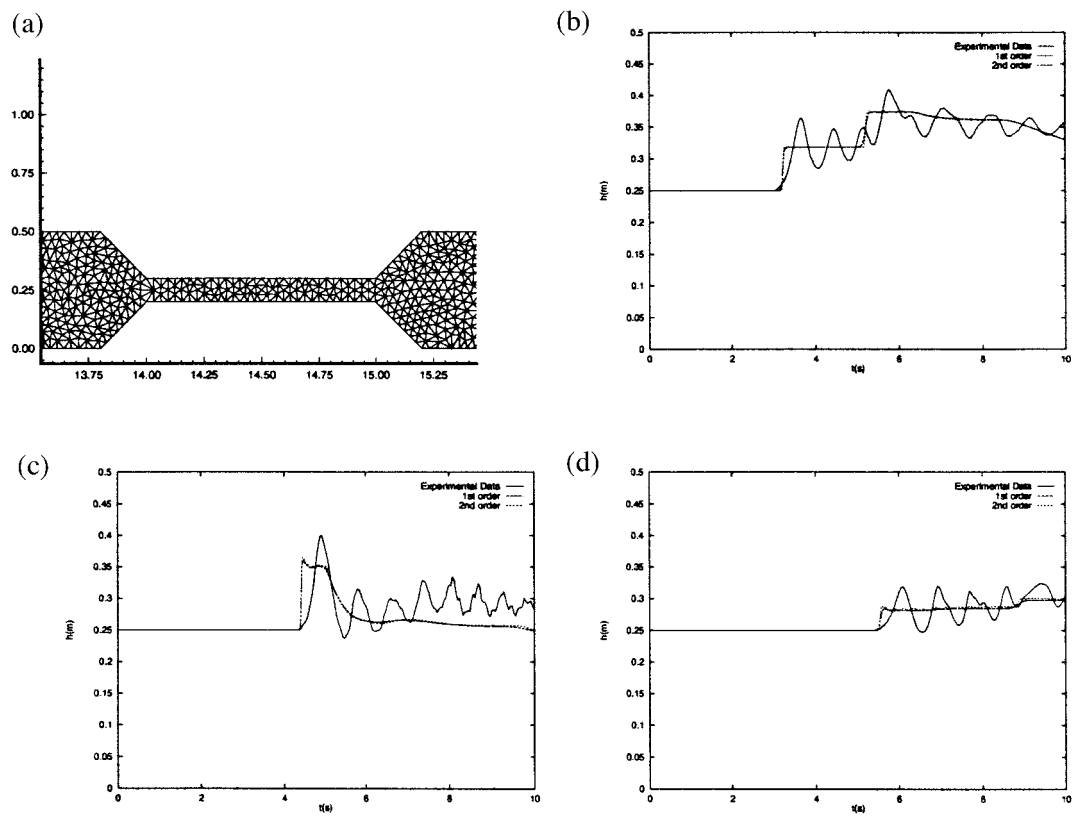

Figure 12. (a) Zoom on the mesh at the constriction, water depth history (b) before the constriction, (c) inside the constriction and (d) after the constriction.

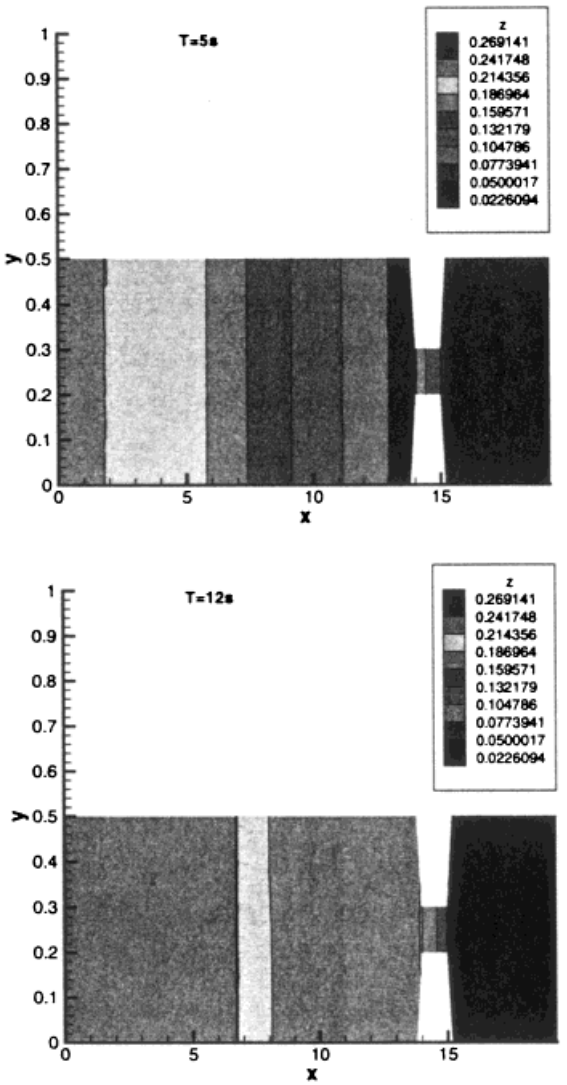

Figure 13. Contour of water level along the channel at time $t = 5$ s (top) and $t = 12$ s (bottom).

for the bottom and the walls is $n_b = n_w = 0.01$ because all the structure was constructed with the same material.

The mesh uses 14207 cells. A zoom on the constriction is shown in Figure 12(a). The front advances and is reflected when it arrives at the constriction. Experimental results are well reproduced by both numerical models. The set of the results are plotted. In Figure 12, the time evolution of the depth of water in different gauging points is represented. Both schemes give

a similar resolution because the mesh is very fine. In both cases, the numerical results predict the water surface lying on an average level over the measured one. This is a consequence of the limitations of the original differential equations that we are solving.

Figure 13 presents the contour level of water at different times, 5 s and 12 s respectively. In Figure 14 the velocity (ten times its real value) is represented at the constriction. Finally, the free surface is plotted along the channel in Figure 15 at the time specified.

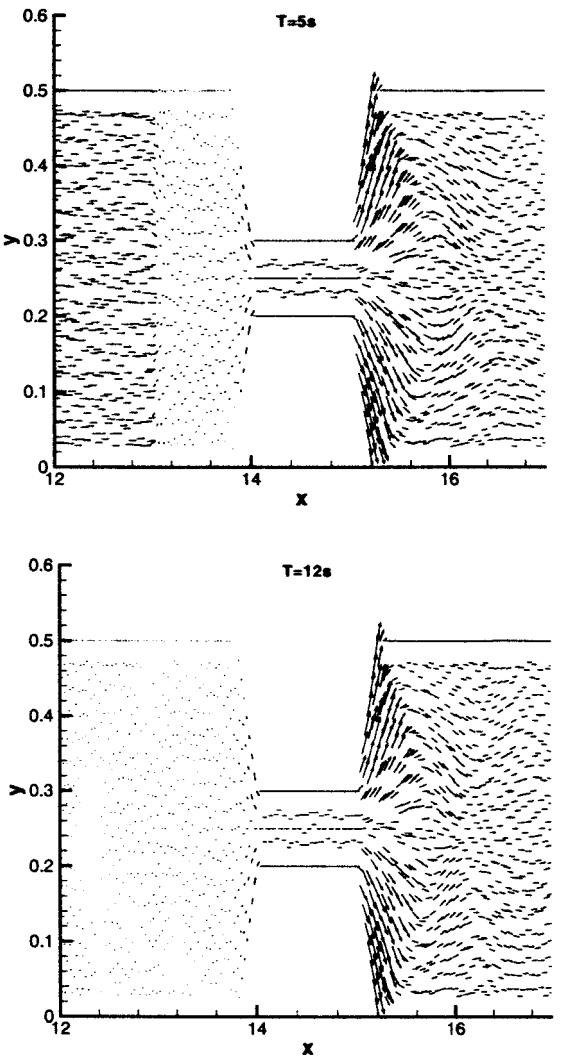

Figure 14. Zoom at the constriction showing the velocity vector at time $t = 5$ s (top) and $t = 12$ s (bottom).

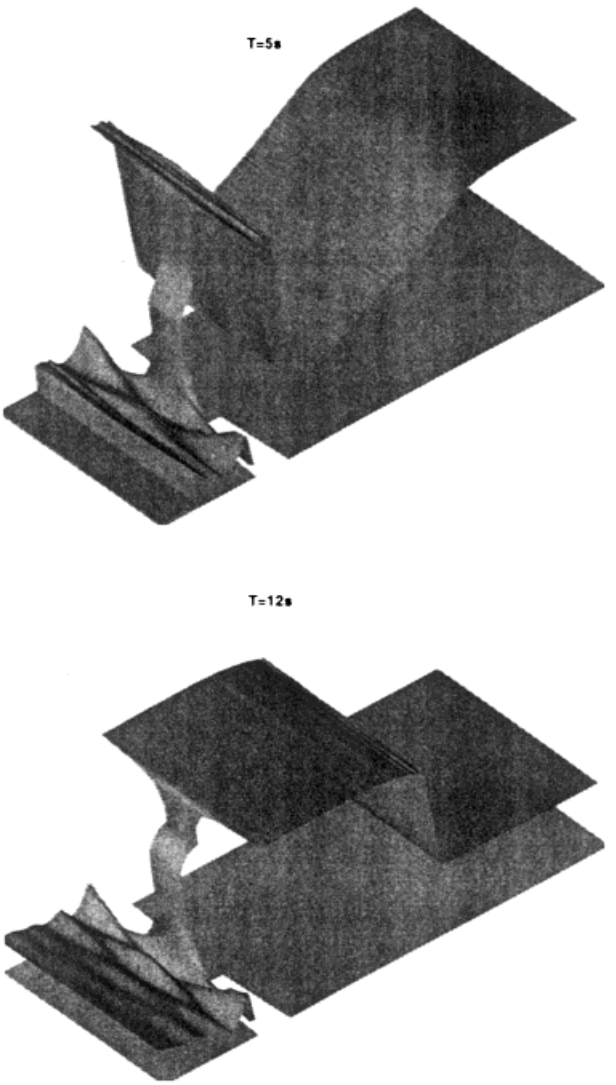

Figure 15. Free surface at time $t = 5$ s (top) and $t = 12$ s (bottom).

5. CONCLUSIONS

An upwind scheme for the solution of the two-dimensional shallow-water equations has been applied in first- and second-order accuracy for dam break modelling. The limiter is defined using a multi-dimensional approach following results developed in the context of gas dynamics [13], instead of generalizations of one-dimensional upwind techniques.

The numerical results have been validated by comparison with experimental data in two test cases involving dam break flows. Differences on the results obtained with first- and second-order accuracy do not follow a clear tendency and it is difficult to establish the superiority of the second-order. In the first test case presented, that of a 45° bend channel, first- and second-order results fail to reproduce the arrival times of the reflected wave (P2 and P3 gauge points). This suggests that the reflection at the corner may require an improved numerical treatment. As future work, the accuracy at boundaries could be an important item to be analysed. In the second test case presented no differences were appreciated since the grid use is very fine.

Modification of the source term to include the vertical side-walls friction effect has supposed a great improvement for the correct prediction of the reflected front. Without using this modified law, the reflected front was detected several seconds after the experimental data.

REFERENCES

1. Alcrudo F, García-Navarro P. A high resolution Godunov-type scheme in finite volumes for the 2D shallow water equations. *International Journal for Numerical Methods in Fluids* 1991; **16**(6): 489–505.
2. Ambrosi D. Approximation of shallow water equations by Roe Riemann solver. *International Journal for Numerical Methods in Fluids* 1995; **20**(2): 157–168.
3. Glaister P. Approximate Riemann solutions of the two-dimensional shallow water equations. *Journal of Engineering and Mathematics* 1990; **24**(1): 45–53.
4. Glaister P. Flux difference splitting for open channel flows. *International Journal for Numerical Methods in Fluids* 1993; **16**(7): 629–654.
5. Louaked M, Hanich L. TVD scheme for the shallow water equations. *Journal of Hydraulic Research* 1998; **36**: 363–378.
6. Harten A. High resolution schemes for hyperbolic conservation laws. *Journal of Computers in Physics* 1983; **49**: 357–393.
7. Roe PL. A basis for upwind differencing of the two-dimensional unsteady Euler equations. In *Numerical Methods in Fluid Dynamics II*. Oxford University Press: Oxford, 1986; 55–80.
8. Bellos CV, Soulis JV, Sakkas JG. Computation of two dimensional dam break induced flows. *Advances in Water Resources* 1991; **14**(1): 31–41.
9. Berzins M, Ware JL. Positive cell-cantered finite volume discretization methods for hyperbolic equations on irregular meshes. *Applications of Numbers and Mathematics* 1995.
10. Brufau P. *An upwind scheme for the 2D shallow water equations with applications*. Numerical Analysis Report 11/97, University of Reading, UK, 1997.
11. Sleigh PA, Berzins M, Gaskell PH, Wright NG. An unstructured finite volume algorithm for predicting flow in rivers and estuaries. *Computers and Fluids* 1997.
12. Osher S, Solomon F. Upwind difference-schemes for hyperbolic systems of conservation laws. *Mathematics and Computers* 1982; **38**(158): 339–374.
13. Batten P, Lambert C, Causon DM. Positively conservative high-resolution convection schemes for unstructured elements. *International Journal for Numerical Methods in Engineering* 1996; **39**: 1821–1838.
14. Wierse M. A new theoretically motivated higher order upwind scheme on unstructured grids of simplicies. *Advances in Computational Mathematics* 1997; **7**: 303–335.
15. Deconinck H, Struijs R, Bourgois G, Paillere H, Roe PL. Multidimensional upwind methods for unstructured grids. *Unstructured Grid Methods for Advection Dominated Flows*, *AGARD* 1992; **787**.
16. García-Navarro P, Hubbard ME, Priestley A. Genuinely multidimensional upwinding for the 2D shallow water equations. *Journal of Computers in Physics* 1995; **121**: 79–93.
17. Hubbard ME. Multidimensional upwinding and grid adaptation for conservation laws. PhD Thesis, University of Reading, UK, 1996.
18. Paillere H. Multidimensional upwind residual distribution schemes for the Euler and Navier–Stokes equations on unstructured grids. PhD Thesis, University of Brussels, Belgium, 1995.
19. Brufau P, García-Navarro P. Two dimensional dam break flows in unstructured grids. Hydroinformatics98, Copenhagen, Denmark, 1998.

20. Abbott MB. *Computational Hydraulics*. Ashgate Publishing Company: UK, 1992.
21. Cunge JA, Holly FM, Verwey A. *Practical Aspects of Computational River Hydraulics*. Pitman: London, 1980.
22. Chow VT. *Open-Channel Hydraulics*. McGraw-Hill: New York, 1959.
23. van Leer B. Towards the ultimate conservative difference scheme III. Upstream-centered finite difference schemes for ideal compressible flow. *Journal of Computers in Physics* 1977; **23**: 263–275.
24. Hirsch Ch. Numerical computation of internal and external flows. In *Computational Methods for Inviscid and Viscous Flows*. Wiley: Chichester, 1990; 2.
25. Durlofsky LJ, Engquist B, Osher S. Triangle based adaptive stencils for the solution of hyperbolic conservation laws. *Journal of Computers in Physics* 1992; **98**: 64–73.
26. Sweby PK. High resolution schemes using flux limiters for hyperbolic conservation laws. *SIAM Journal of Numerical Analysis* 1984; **21**: 995–1011.
27. Molls T, Zhao G, Molls F. Friction slope in depth-averaged flow. *Journal of Hydraulic Engineering* 1998; **124**(1): 81–85.
28. Berger RC, Stockstill RL. Finite-element model for high-velocity channels. Journal of Hydraulic Engineering. *ASCE* 1995; **121**(10): 710–716.
29. Chaudhry MH. *Open-Channel Flow*. Prentice-Hall: Englewood Cliffs, NJ, 1993.
30. Fennema RJ, Chaudhry MH. Explicit methods for 2D transient free surface flows. *Journal of Hydraulic Engineering* 1990; **116**: 1013–1034.
31. Zhao DH, Shen HW, Tabios GQ, Lai JS, Tan WY. Finite-volume two-dimensional unsteady-flow model for river basins. Journal of Hydraulic Engineering. *ASCE* 1994; **120**(7): 863–883.

